Journal of Quantitative Spectroscopy & Radiative Transfer 221 (2018) 38–50

Contents lists available at ScienceDirect

Journal of Quantitative Spectroscopy & Radiative Transfer

journal homepage: www.elsevier.com/locate/jqsrt

A pilot study of shortwave spectral fingerprints of smoke aerosols above liquid clouds

Xiaoguang Xu[a,b,*], Jun Wang[a,*], Jing Zeng[a], Weizhen Hou[a], Kerry G Meyer[c], Steven E Platnick[c], Eric M Wilcox[d]

[a] Department of Chemical and Biochemical Engineering, Center of Global and Regional Environmental Studies, and Informatics Initiative, University of Iowa, Iowa City, IA, USA
[b] Now at Joint Center for Earth Systems Technology, University of Maryland at Baltimore County, Baltimore, MD, USA
[c] Climate and Radiation Lab, NASA Goddard Space Flight Center, Greenbelt, USA
[d] Desert Research Institute, Reno, NV, USA

ARTICLE INFO

Article history:
Received 8 May 2018
Revised 24 September 2018
Accepted 24 September 2018
Available online 25 September 2018

ABSTRACT

Absorbing aerosols like smoke heat the atmosphere by absorbing solar radiation, and such heating is enhanced when aerosols are above liquid clouds. To reduce uncertainty in estimates of the aerosol radiative forcing, it is desirable to characterize the size, index of refraction, optical depth, and altitude of smoke aerosols and underlying cloud droplets. While past work with remotely sensed multi-spectral data have made progress toward such characterization, it remains unclear if those radiatively important parameters can be fully and simultaneously retrieved from shortwave hyperspectral measurements. This issue is studied here first by examining the spectral fingerprints of above-cloud aerosols in the shortwave region (wavelength from 330 nm to 4000 nm) using hyperspectral radiative transfer simulations. These simulations are further explored to analyze the information content for hyperspectral inversion of aerosol and cloud optical depths as well as their microphysical properties over an ocean surface. The analysis shows that the Moderate Resolution Imaging Spectroradiometer (MODIS), with limited spectral bands in the solar spectrum, has partial information required for retrieving the optical depth and the effective radius of smoke and cloud. In contrast, hyperspectral measurements have about 5 extra pieces of information (double the degrees of freedom for signals of MODIS), allowing for the retrieval of additional aerosol and cloud microphysical parameters, including the smoke layer height above cloud, the imaginary part of smoke refractive index, and partially the effective variance of cloud droplet size. Thus, hyperspectral measurements can provide valuable constraints on heating rate estimates of absorbing aerosols above clouds.

1. Introduction

Over the past decade, the role of above-cloud aerosols (ACA) in affecting regional and global climate has been increasingly appreciated (e.g., [7,30,64,65,72]). This is in particular the case for smoke aerosols that can heat the atmosphere by absorbing solar radiation, and such heating is enhanced when the smoke plume is above a liquid cloud layer [21,65]. During each boreal summer to fall, thick smoke aerosols produced by biomass burning (BB) in Southern Africa and South Asia travel downwind and frequently overlay long-lasting subtropical stratocumulus decks over the southeast Atlantic Ocean and south Asia, respectively. Statistically, the frequency of occurrence of these ACA events in an overcast sky reaches up to 50% in southeast Atlantic and 10% in South Asia [1,2,16].

In particular, smoke emitted in Southern Africa contributes about one third of the global BB aerosols [12,59], the prevailing ACAs thus exert significant regional radiative warming to the atmosphere. The monthly average of conditional TOA direct radiative forcing of ACAs was estimated as 20–35 Wm^{-2} [7,8,15,74] and the instantaneous forcing can be greater than 100 Wm^{-2} for extremely dense absorbing smoke plumes [15,20]. If considering all-sky conditions, the ACAs over this region can contribute about 0.02 Wm^{-2} to global radiative forcing [44]. Despite the importance of ACAs, quantification of ACA's radiative effects in climate models remains considerably uncertain. A recent comparison of global

---

[*] Corresponding author at: Department of Chemical and Biochemical Engineering, Center of Global and Regional Environmental Studies, and Informatics Initiative, University of Iowa, Iowa City, IA, USA.

E-mail addresses: xiaoguang-xu@uiowa.edu (X. Xu), jun-wang-1@uiowa.edu (J. Wang).

https://doi.org/10.1016/j.jqsrt.2018.09.024

climate models saw the largest inter-model differences of all-sky direct radiative forcing in southeast Atlantic, with the modelled annual mean values varying from -1 to $+2$ Wm^{-2} [42].

The presence of ACAs also affects satellite remote sensing of cloud properties. When a cloud pixel is contaminated by lofted smoke aerosols, the TOA reflectance as observed by a satellite sensor is reduced and the spectral contrast increases. As a result, the retrieved cloud properties are biased if such smoke influence is not considered. For instance, a low bias of 6–20% was identified in the standard cloud optical depth (COD) retrievals from the Moderate Resolution Imaging Spectroradiometer (MODIS) when smoke aerosols aloft [1,37,66]; cloud droplet effective radius could also be underestimated by 1 µm or less [25,37,66]. Consequently, the presence of ACAs can lead to biased satellite-based estimates of cloud liquid water content and radiative effect [37,65].

In order to better understand the radiative effects of ACA and to improve the retrieval of cloud properties in smoke-contaminated scenes, a technique has been developed to derive properties of cloud and ACA simultaneously by utilizing the spectral signatures of ACA. The technique is known as “color ratio”, which physically takes advantage of the unambiguous reduction of spectral TOA reflectance due to enhanced absorption of sunlight by ACA [e.g., [28,38,58]]. For instance, Torres et al. [58] retrieved COD and ACA AOD from 388-nm TOA reflectance and ultraviolet (UV) absorbing aerosol index (between 388 nm and 353 nm) observed by the Ozone Monitoring Instrument (OMI), whereas Jethva et al. [28] retrieved the same variables using the color ratio of 470 nm and 860 nm made by MODIS-measured TOA reflectance. Meyer et al. [38] further used reflectance measurements at six MODIS channels in the solar spectrum to retrieve COD, ACA AOD, and cloud droplet effective radius. Their retrieval accuracy, however, depends critically on the imaginary part of smoke refractive index, which determines single scattering albedo (SSA) for a given particle size distribution, and aerosol-cloud relative altitude. As highlighted by Jethva et al. [28], an error of 0.03 in the SSA or 1 km in the aerosol-cloud relative altitude could led to an error of 10–50% or 15% in the retrieved ACA AOD, respectively.

Therefore, it is necessary to explore the potential of retrieving the full set of cloud and ACA parameters that are important for studying the radiative effects of ACAs. While spectral COD and ACA AOD are important for radiative transfer calculations, equally important but poorly constrained are the effective size of smoke particles and cloud droplets, the spectral single scattering albedo (or refractive index) of smoke, and the relative height of the smoke above cloud layers. By investigating spectral fingerprints of above-cloud smoke aerosols using radiative transfer simulations, this study aims to assess the capability for hyperspectral inversion of optical thickness of both aerosol and cloud, along with their microphysical properties and vertical separation over an ocean surface. In particular, this study examines how the information brought by hyperspectral measurements compares with multi-band data such as those offered by the MODIS instrument.

2. Methodology

The framework used to assess retrievable information combines a linearized vector radiative transfer model and an optimal estimation (OE) approach. The model, known as Unified Linearized Vector Radiative Transfer Model (UNL-VRTM) [61], simulates reflectance being observed by any satellite for an atmosphere with specified cloud and aerosol properties. It also diagnoses analytical Jacobians of reflectance at top of the atmosphere (TOA) with respect to aerosol and cloud variables. The OE method is then used to evaluate the information content of the synthetic TOA reflectance and estimate the expected retrieval uncertainties in cloud and aerosol properties. To reduce the number of retrieved parameters, the principal component analysis (PCA) technique is applied to identify primary components in the spectral variation of aerosol refractive index.

In this section, we first describe the information analysis theory (2.1) and UNL-VRTM (2.2), then describe cloud and aerosol microphysical properties used for generating synthetic hyperspectral and MODIS-type data (2.3–2.4). *New* development of computing Jacobians of Stokes parameters with respect to weight coefficients for each principal components (PCs) of aerosol spectral refractive index is presented in 2.5. The state vector and its prior errors are defined in 2.6. At last, the approach to characterize observation error covariance is presented in 2.7.

2.1. Information theory

We apply a Bayesian-based OE approach to quantify the pieces of useful information contained in the observation for inferring a set of unknown parameters [48]. This approach has been extensively used to analyze aerosol information of remote sensing observations [e.g., 9,26,69]. A detailed description of this approach was presented by Xu and Wang [69]. Here we introduce it briefly.

Let $\mathbf{x} = [x_1, \cdots x_N]^T$ denote a state vector that contains N parameters to be retrieved, $\mathbf{y} = [y_1, \cdots y_M]^T$ denote an observation vector with M elements of measurements, and $\mathbf{K}$ represents the Jacobian matrix of $\mathbf{y}$ with respect to $\mathbf{x}$. Assuming a linear relationship between $\mathbf{y}$ and $\mathbf{x}$ in their vicinities, such relation can be expressed by

$$\mathbf{y} = \mathbf{K}\mathbf{x} + \epsilon, \tag{1}$$

where ϵ is an experimental error that includes observation noise and forward modeling uncertainty. For this project, the observation vector $\mathbf{y}$ comprises spectral reflectance, and the state vector $\mathbf{x}$ comprises a variety of cloud and aerosol variables. The inverse problem is to solve $\mathbf{x}$ from the measurement $\mathbf{y}$, and the solution (or the retrieval) is denoted by $\hat{\mathbf{x}}$.

Assuming that prior error and observation error are characterized by a Gaussian probability distribution function (PDF), one can estimate the posterior error by

$$\hat{\mathbf{S}} = \left(\mathbf{K}^T\mathbf{S}_\epsilon^{-1}\mathbf{K} + \mathbf{S}_\mathrm{a}^{-1}\right)^{-1}, \tag{2}$$

where $\mathbf{S}_\epsilon$ is the observation error covariance matrix, $\mathbf{S}_\mathrm{a}$ is error covariance matrix of prior estimates of the state vector $\mathbf{x}_\mathrm{a}$. The retrieval error in $\hat{\mathbf{x}}$ can be estimated by the root-mean-square of the main diagonal of $\hat{\mathbf{S}}$,

$$\hat{\epsilon} = [\mathrm{diag}(\widehat{\mathbf{S}})]^{\frac{1}{2}}. \tag{3}$$

Accordingly, the averaging kernel matrix $\mathbf{A}$ is defined by

$$\mathbf{A} = \left(\mathbf{K}^T\mathbf{S}_\epsilon^{-1}\mathbf{K} + \mathbf{S}_\mathrm{a}^{-1}\right)^{-1}\mathbf{K}^T\mathbf{S}_\epsilon^{-1}\mathbf{K}. \tag{4}$$

$\mathbf{A}$ describes the ability to retrieve $\mathbf{x}$ from $\mathbf{y}$ given the error characterizations of observation and $\mathbf{x}_\mathrm{a}$. An identity matrix of $\mathbf{A}$ represents a perfect retrieval, while a null matrix of $\mathbf{A}$ indicates that no information can be gained from $\mathbf{y}$. The trace of $\mathbf{A}$ is known as the degree of freedom for signals, or DFS for short,

$$\mathrm{DFS} = \mathrm{trace}(\mathbf{A}). \tag{5}$$

DFS represents independent pieces of information retained by the observation. The diagonal elements of $\mathbf{A}$, being called partial DFS or DFS$_i$, with a value between 0 and 1, indicate the partial capability to retrieve each individual parameter,

$$\mathrm{DFS}_i = \mathrm{diag}(\mathbf{A})_i = \frac{\partial \hat{x}_i}{\partial x_i}. \tag{6}$$

Table 1
Model settings and parameters assumed but not included in the state vector.

Parameter	Setting
Atmospheric profile	Tropical standard atmosphere [36]
Surface reflectance	Water surface from ASTER spectral library [3]
Cloud altitude range	1–2 km
Smoke altitude range	2–8 km
Particle shape	Sphere for both smoke aerosols and cloud droplets
Cloud refractive index	From Hale and Querry [22], Downing and Williams [18], and Kou et al. [33].
PCs of smoke refractive index	Obtained through PCA to smoke database of Magi et al. [35]

2.2. UNL-VRTM

We use the UNL-VRTM (https://unl-vrtm.org) to perform hyperspectral radiative transfer simulations. As described by Wang et al. [61], UNL-VRTM integrates the VLIDORT radiative transfer code [53], linearized Mie and T-Matrix scattering codes [55], HITRAN gaseous spectroscopic database [50], reflection models of land and water surfaces [52], and the OE-based information assessment module [69]. Together, these components constitute a numerical testbed tool for satellite remote sensing of the atmosphere by offering analytical Jacobians of radiation fields and quantitative information content of any instrumental measurements.

In this study, our UNL-VRTM simulations consider two scenarios of satellite observations for the purpose of assessing the additional information brought by hyperspectral measurements. One represents a shortwave spectrometer with a resolution (in terms of full width at half-maximum, or FWHM) of 5 cm^{-1} measuring radiances in the wavenumbers between 2500 and 30,000 cm^{-1} (wavelengths of 333–4000 nm). In the wavelength space, such a spectral resolution corresponds to about 0.055 nm at the wavelength of 333 nm, 0.5 nm around 1000 nm, 2 nm around 2000 nm, and 8 nm around 4000 nm. This type of instrument is similar to the spectrometer designed for the CALRREO and CLARREO Pathfinder missions [56,63] but with a higher spectral resolution. The second scenario considers observations corresponding to multi-spectral radiometers such as MODIS. Among MODIS's 36 channels, 12 channels falling within our simulated spectral range are considered, i.e. channels 1–7, 17–21, and 26. It should be noted that MODIS ocean color channels (8–16) are not selected as they are tuned for dark scenes and often saturated over clouds.

For both the spectral scenarios, we only consider the at-nadir observations over a water surface at a constant solar zenith angle of 40°. Surface reflectance is obtained from the ASTER spectral library [3] and assumed isotropic, above which is a standard tropical atmosphere with 49 layers [36]. Based on the standard atmosphere's vertical profile of air density, UNL-VRTM calculates air molecular scattering properties following Bodhaine et al. [4]. Absorption of trace gases are calculated using the recently updated HITRAN2012 database [49] for 22 gases including H_2O, CO_2, O_3, N_2O, etc. It also includes continuum absorption by H_2O, CO_2, O_3, and O_2 using the MT_CKD approach [11,40].

A homogeneous deck of stratocumulus cloud present between 1 and 2 km with smoke particles aloft between altitudes of 2 and 8 km. Smoke extinction profile follows a quasi-Gaussian shape characterized by a median altitude of 5 km with peak extinction and a dispersion half-width of 1 km [54,70]. As such, the effective separation distance between cloud top and smoke layer is 3 km. We assume an optical thickness of 10 for the cloud layer and 0.5–1.0 for the smoke layer at the spectral wavelength of 550 nm. Optical properties of cloud and smoke are determined using Lorenz–Mie scattering theory based on the microphysical variables presented in the following subsections. Table 1 summarizes the assumed model settings and parameters that are not included in the state vector.

2.3. Cloud microphysical and optical properties

Microphysical properties of cloud droplets are described by the size distribution and refractive index. Many studies have suggested cloud droplets follow a modified Gamma distribution characterized by an effective radius $r^{\mathrm{c}}_{\mathrm{eff}}$ and an effective variance $\nu^{\mathrm{c}}_{\mathrm{eff}}$ [24],

$$n_{\mathrm{c}}(r) = N_{\mathrm{c}} r^{(1/\nu^{\mathrm{c}}_{\mathrm{eff}}-3)} \exp\left(-\frac{r}{r^{\mathrm{c}}_{\mathrm{eff}}\nu^{\mathrm{c}}_{\mathrm{eff}}}\right), \tag{7}$$

where N_{c} is a constant related to the total number of droplets per unit volume. For marine stratocumulus, typical values of $r^{\mathrm{c}}_{\mathrm{eff}}$ and $\nu^{\mathrm{c}}_{\mathrm{eff}}$ are around 10 µm and 0.1, respectively [39,43]. Complex refractive index of liquid water in the shortwave is based on the widely used databases reported by Hale and Querry [22], Downing and Williams [18], and Kou et al. [33] to cover the entire spectral range of this study. As displayed in Fig. 1a and b, the real part of water refractive index is about 1.33 in visible, decreases with the wavelength in near infrared (NIR), and reaches its minimum in shortwave IR (SWIR) around 2.7 µm before a rapid increase towards medium-wave IR (MWIR). The imaginary part is negligibly small in the visible bands and increases dramatically as the wavelength increases. Additionally, these refractive index datasets overlap in the near-infrared through shortwave infrared, and discrepancies exist in some regions mainly due to differences in the spectral sampling resolution. Our selection of dataset in the overlapped spectrum favors the data of Kou et al. [33] and followed by that of Downing and Williams [18].

Fig. 1c and d presents cloud SSA and extinction COD as a function of spectral wavelength. Spectral CODs are determined using the droplet volume that gives a COD of 10 at the wavelength of 550 nm. The spectral variability of COD is small with an increase of up to about 10% at from visible to shortwave infrared wavelengths. Cloud SSA is almost equal to 1 at wavelengths shorter than 1.3 µm. In contrast, clouds have a strong absorption signature at wavelengths around 1.35, 2.0, and 2.5–3.5 µm. It should be noted that the absorption signature of clouds is not quite useful for remote sensing of cloud properties, except the 1.35 µm band which overlaps with strong absorption of water vapor and contains information for the height of clouds.

2.4. Smoke microphysical and optical properties

Smoke particles are assumed to follow a lognormal size distribution characterized by a median radius r_{g} and standard deviation σ_{g}, which is expressed by

$$n_{\mathrm{a}}(r) = \frac{N_{\mathrm{a}}}{\sqrt{2\pi}\; r \ln\sigma_{\mathrm{g}}} \exp\left[-\frac{(\ln r - \ln r_{\mathrm{g}})^2}{2\ln^2\sigma_{\mathrm{g}}}\right] \tag{8}$$

An advantage of the lognormal distribution is that the σ_{g} is identical for the number, area, and volume size distribution functions, and therefore the corresponding median radius of each distribution function can be derived from one to another [24]. Furthermore, effective size variables (i.e., $r^{\mathrm{a}}_{\mathrm{eff}}$ and $\nu^{\mathrm{a}}_{\mathrm{eff}}$) can also be converted to and from those geometric parameters [71]. Following Xu

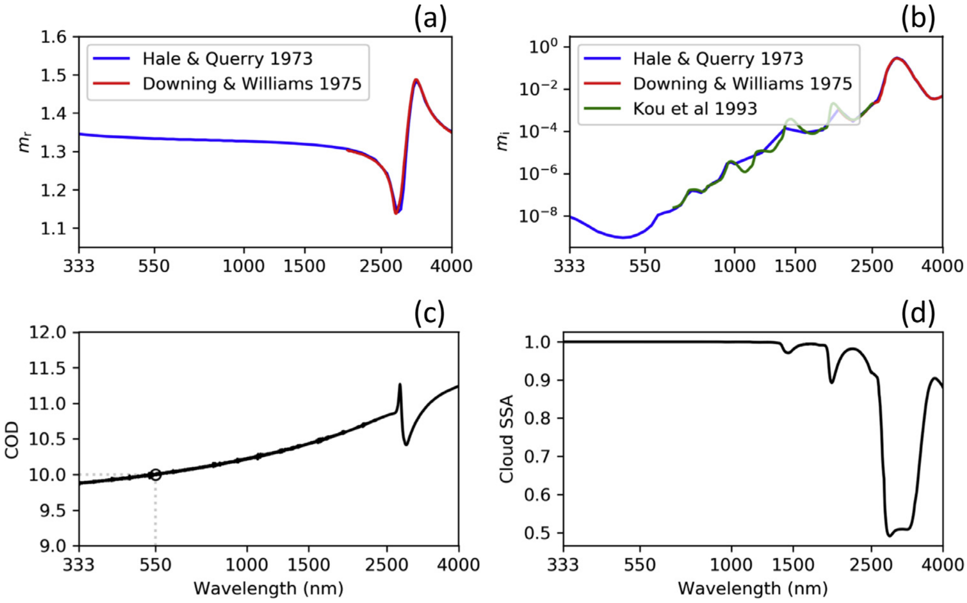

Fig. 1. Cloud droplet refractive index and optical properties adopted in this study. (a-b) Refractive indices of liquid water ($m_r^c - m_i^c i$) reported by Hale and Querry [22] at the temperature of 298 K (blue), *Downing and Williams* [18] at 300 K (red), and *Kou* et al. [33] at 295 K (green). (c-d) Simulated cloud optical depth (or COD, a value of 10 is specified at a wavelength of 550 nm) and single scattering albedo (SSA) using a Lorenz-Mie code. (For interpretation of the references to color in this figure legend, the reader is referred to the web version of this article.)

et al. [71], we use $r_{\mathrm{eff}}^{\mathrm{a}}$ and $\nu_{\mathrm{eff}}^{\mathrm{a}}$ for our experiment because aerosol particles following different size distributions function but having the same values of r_{eff} and ν_{eff} possess similar scattering and absorption properties [24].

In contrast to the well-characterized water refractive index, refractive index of smoke aerosols is highly uncertain due to the complexity of smoke's chemical compositions as the aging of plume. Furthermore, measurements of smoke refractive index on the entire shortwave spectrum are very limited. In this study, we use spectral refractive indices in UV to NIR inferred by Magi et al. [35] (hereafter, Magi07) for six biomass burning plumes during the SAFARI-2000 field campaign. As shown in Fig. 2a and b, both the real and imaginary parts of smoke refractive index vary strongly with spectral wavelength and differ significantly among different smoke plumes. Fig. 2c and d shows the spectral AOD (normalized to 0.5 at spectral wavelength of 550 nm), SSA, and absorption AOD (AAOD). The spectral AOD decreases along with wavelength, and at 1560 nm it decreases to about 10% of that at 550 nm. The variability of smoke AAOD displays strong case-dependency, highlighting the necessity for determining the imaginary part refractive index.

2.5. Principal components (PCs) of smoke refractive indices

We assume the spectral signal of smoke refractive index can be decomposed into several orthogonal PCs multiplied by a vector of weighting coefficients. These PCs are predetermined through PCA applied to a set of known refractive spectra. The retrieval targets then become the weighting coefficients, from which the spectral refractive indices can be reconstructed. By doing so, the size of state vector is significantly reduced and, at the same time, the intrinsic band-to-band correlations of refractive index are adopted. Suppose a refractive index dataset contains a number of samples with each recorded at d wavelengths, application of PCA to the dataset provides a matrix of orthogonal PCs ($\mathbf{P}$). Conversely, a spectrum of refractive index ($\mathbf{r}$) can be approximated from $\mathbf{P}$ by

$$\mathbf{r} = \mathbf{P}\mathbf{w}, \tag{9}$$

where $\mathbf{w}$ represents a vector of m weighting coefficients. Usually a small number of m is sufficient to reconstruct $\mathbf{r}$ with a sufficient accuracy. In this study, we apply PCA to the Magi07 datasets. As shown in Fig. 3a and b, the first 3 PCs ($m = 3$) can describe over 99% of the spectral variability for both the real and imaginary parts. As a consequence, the spectral refractive index can be reconstructed well using these first 3 PCs (Fig. 3c and d).

Following our previous efforts in realizing the PCA-based surface reflectance [26,27], we implemented the capability in UNL-VRTM to calculate the Jacobian of the TOA reflectance (R) with respect to weighting coefficients ($\mathbf{w}$) of PCs of aerosol refractive index, which can be expressed by

$$\frac{\partial R}{\partial \mathbf{w}} = \frac{\partial R}{\partial r_{\lambda_i}}\left[P_{i,1}, P_{i,2}, \cdots, P_{i,m}\right]^T, \quad (i = 1, \cdots, d). \tag{10}$$

Here $\frac{\partial R}{\partial r_{\lambda_i}}$ indicates Jacobian gradients of TOA reflectance to refractive index at wavelength of λ_i, which are explicitly calculated by UNL-VRTM. $P_{i,\,m}$ represents the mth PC at wavelength λ_i, acquired through applying PCA to the Magi07 datasets.

2.6. Definition of state vector and prior error

The state vector comprises 13 cloud and aerosol parameters listed in Table 2. They are 550-nm COD (τ_{550}^{c}), cloud droplet effective radius ($r_{\mathrm{eff}}^{\mathrm{c}}$) and effective variance ($\nu_{\mathrm{eff}}^{\mathrm{c}}$); ACA AOD at 550 nm ($\tau_{550}^{\mathrm{a}}$), aerosol effective radius ($r_{\mathrm{eff}}^{\mathrm{a}}$) and effective variance ($\nu_{\mathrm{eff}}^{\mathrm{a}}$); complex aerosol refractive index represented by a set of 3 PC coefficients ($\mathbf{w} = [w_1,\ w_2,\ w_3]$, each for real and imaginary parts); aerosol-cloud separation height (H). Therefore, the state vector can be expressed by

$$\mathbf{x} = \left[\tau_{550}^{\mathrm{c}},\ r_{\mathrm{eff}}^{\mathrm{c}},\ \nu_{\mathrm{eff}}^{\mathrm{c}},\ \tau_{550}^{\mathrm{a}},\ r_{\mathrm{eff}}^{\mathrm{a}},\ \nu_{\mathrm{eff}}^{\mathrm{a}},\ H,\ w_{\mathrm{r},1},\ w_{\mathrm{r},2},\ w_{\mathrm{r},3},\ w_{\mathrm{i},1},\ w_{\mathrm{i},2},\ w_{\mathrm{i},3}\right]^T. \tag{11}$$

In the radiative transfer simulation, COD and AOD at other wavelengths are calculated from cloud and aerosol volume concentrations that converted from τ_{550}^{c} and τ_{550}^{a}. In other words, spectral variability of cloud and aerosol optical depths is governed by their

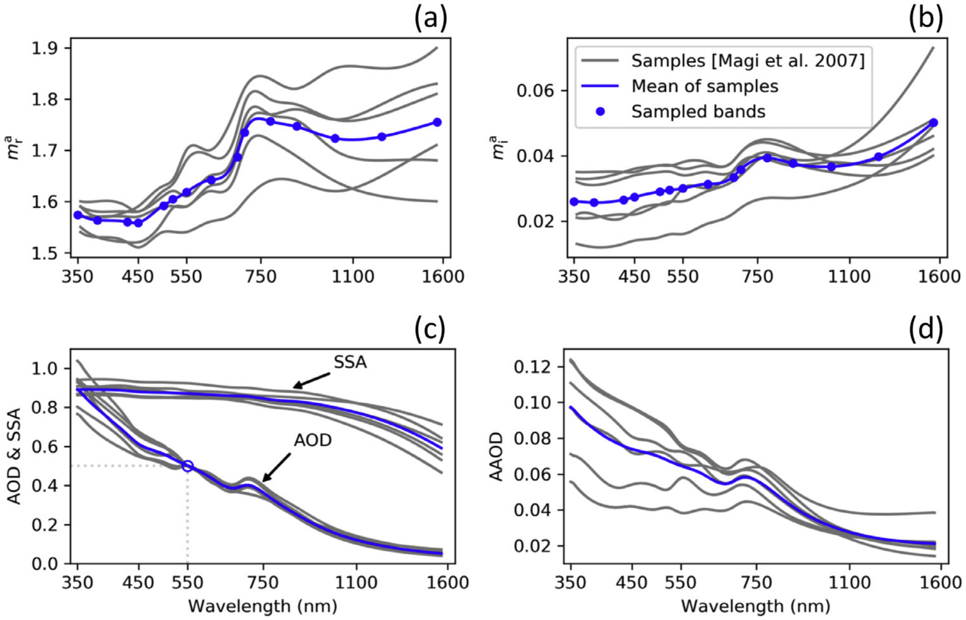

Fig. 2. Smoke aerosol refractive index and optical properties adopted in this study. (a-b) Refractive indices ($m_r^a - m_i^a i$) retrieved by Magi et al. [35] (grey curves) for smoke plumes observed during the SAFARI- 2000 campaign. The blue curve represents average of these six samples. (c) Simulated aerosol optical depth (AOD, a value of 0.5 is specified at the wavelength of 550 nm) and SSA using the mean spectra of smoke refractive index. (d) Absorption AOD (or AAOD) of smoke. (For interpretation of the references to color in this figure legend, the reader is referred to the web version of this article.)

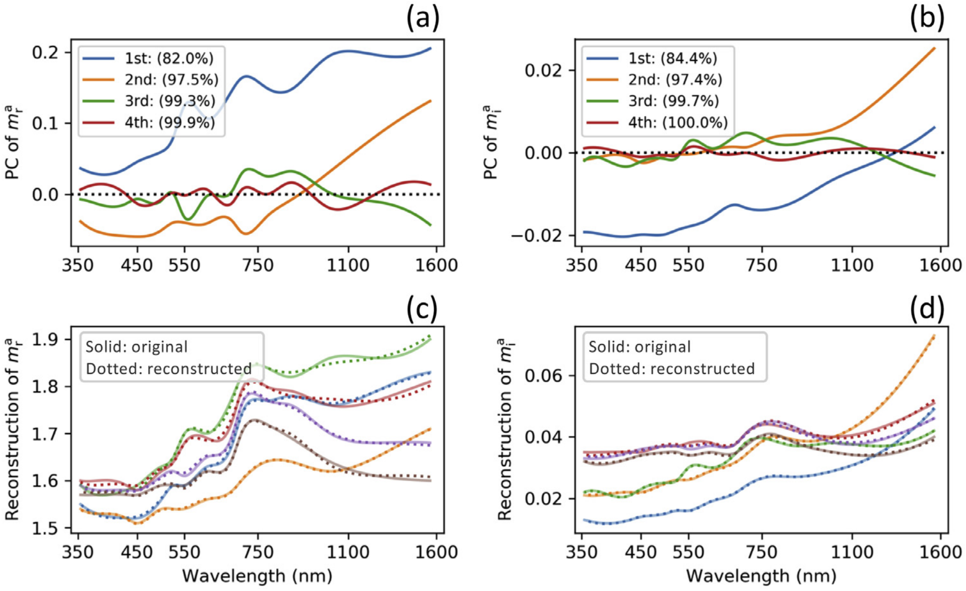

Fig. 3. Principal component analysis applied to smoke refractive index spectra of Magi et al. [35]. (a-b) The first 4 principal components (PCs) and their cumulative variance competitions. (c-d) Comparisons of reconstructed refractive index spectra (dotted) using the first 3 PCs to the original spectra (solid). .

microphysical parameters, and τ_{550}^c and τ_{550}^a can be treated as the cloud and aerosol loading parameters independent of other parameters in the state vector. In addition, microphysical parameters, as well as PC weights, in the state vector are independent of each other. Therefore, we neglect correlations between prior errors by assuming a diagonal prior error covariance matrix $\mathbf{S}_a$.

Table 2 presents the adopted value for each parameter in the state vector, as well as the estimated prior uncertainty. As mentioned earlier, we consider a thick cloud layer with $\tau_{550}^c = 10$ presenting between 1 and 2 km altitudes. Cloud typical r_{eff}^c of 10 µm and v_{eff}^c of 0.1 are selected according to Miles et al. [39] and Nakajima et al. [43]. We assume a relative prior error of 50% for τ_{550}^c and r_{eff}^c. This assumes that one can get COD with a 50% uncertainty from other sources. The uncertainty for r_{eff}^c is consistent to Nakajima et al. [43] who found the retrieved effective radii for marine stratocumulus were generally between 5 µm and 15 µm. Prior uncertainty of v_{eff}^c is assumed 100% according to the variability of this parameter reported by Miles et al. [39] (Note Mile et al. [39] used a different form of Gamma distribution function).

The overlaid smoke extends between the altitudes of 2 km and 8 km following a quasi-Gaussian shape. Vertically, its extinction peaks at an altitude of 5 km. The relative height of smoke above cloud is thus 3 km, i.e., $H = 3$ km. Such height corresponds to a typical ACA phenomenon — smoke layers over the southern At-

Table 2
Adopted state vector values (x_a) and prior errors (ϵ_a)*.

	Cloud parameters			Smoke parameters				PC weights of refractive index					
	τ^c_{550}	r^c_{eff} (μm)	v^c_{eff}	H(km)	τ^a_{550}	r^a_{eff} (μm)	v^a_{eff}	$w_{r,1}$	$w_{r,2}$	$w_{r,3}$	$w_{i,1}$	$w_{i,2}$	$w_{i,3}$
x_a	10.0	10.0	0.1	3.0	0.5	0.12	0.18	0.0	0.0	0.0	0.0	0.0	0.0
ϵ_a	5.0	5.0	0.05	2.0	0.4	0.10	0.10	3.35	1.46	0.49	0.43	0.17	0.07

lantic were often located between 2 km and 6 km as detected by the satellite lidar [12]. Das et al. [12] also suggested smoke layer height can vary by about 2 km spatially. Thus, we assume a prior uncertainty of 2 km for H. Smoke r^a_{eff} (0.12 µm) and v^a_{eff} (0.18), as well as their prior errors (0.1 µm and 0.1, respectively), were determined from long-term measurements of biomass burning aerosols by the Aerosol Robotic Network [19]. Prior estimates for PC weights of refractive index are zeros, which give the mean spectra of the Magi07 refractive indices. Their uncertainties listed in Table 2 are the standard deviations of the weights for reconstructing Magi07 samples, which describe the variability of smoke refractive index observed from different plumes.

2.7. Observation error covariance matrix

Usually, observation errors include instrument noises and forward model errors. Observation error covariance matrix thus have two terms,

$$\mathbf{S}_\epsilon = \mathbf{S}_y + \mathbf{S}_m, \tag{12}$$

where $\mathbf{S}_y$ is error covariance matrix describing the instrument noises, and $\mathbf{S}_m$ indicates covariance matrix of forward model errors. Here, we assume that TOA reflectance has a relative instrument error of 2% with a lower cap of 0.002. For hyperspectral data, inter-channel correlations of instrument noises are limited to 5 adjacent channels on either side, with correlation coefficients decrease from 0.95 to 0.20. While we are not deal with any specific instrument, this assumption of inter-channel error is to reconcile spectral resolutions of some existing and future spectrometers. For example, AVIRIS-NG (the Airborne Visible/Infrared Imaging Spectrometer – Next Generation) measures the wavelength range from 380 nm to 2510 nm with 5 nm sampling and resolution (FWHM) [https://aviris-ng.jpl.nasa.gov]; CLARREO spectrometer measures the spectral range of 320–2300 nm with 4-nm sampling interval and 8-nm FWHM [63]; TEMPO (the Tropospheric Emissions: Monitoring Pollution mission) measures UV and visible at 0.6-nm FWHM; TROPOMI (the Tropospheric Monitoring Instrument) has FWHM of ~ 0.5 nm in UV and visible, 0.35 nm in NIR, and 0.225 nm in SWIR. We assume a same $\mathbf{S}_m$ for MODIS-like data but excluding the inter-channel correlations.

Model error represents the uncertainties in the forward model, which usually caused by errors in model assumptions and inaccurate parametrizations. In practice, it is difficult to analytically derive $\mathbf{S}_m$ due to the complexity of the model. A traditional way is to estimate it by the Monte Carlo method, a widely used approach in data assimilation for numerical weather predictions [5]. This method precedes in three steps. First, a variety of relevant model parameters are randomly perturbed within their error ranges. Second, an ensemble of forward simulations are performed with input of perturbed parameters. Lastly, a covariance matrix is calculated from the ensemble simulations, which can be used to approximate $\mathbf{S}_m$. In this study, some perturbed parameters are those that may significantly affect the TOA reflectance simulation but are not included in the state vector. Those parameters (and error magnitude) are solar zenith angle (0.1°), viewing zenith angle (0.1°), surface reflectance (0.01), surface pressure (10 hPa), aerosol top altitude (2 km), real part (0.01) and imaginary part (3%) of cloud droplet refractive index, and columnar amounts of water vapor (5%) and O_3 (5%). In addition, perturbed variables also include some model parameters in the state vector, i.e., COD (2%), AOD (4%), r^c_{eff} (2%), and r^a_{eff} (4%). Such a consideration is to account for error sources that are difficult to represent, which include but not limited to heterogeneity of the distribution and size of clouds and aerosols [13]. The uncertainties of those perturbed parameters (bracketed values) are used to seed the perturbed samples, generally representing accuracies that can be achieved from relevant sources.

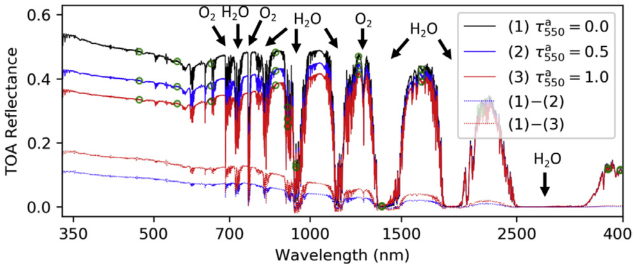

Fig. 4. TOA reflectance simulated by UNL-VRTM for cloud-only (black) and for two scenarios of over-cloud smoke with 550-nm AOD of 0.5 (solid blue) and 1.0 (solid red). Discontinuities in the reflectance spectra result from absorption of solar radiation by water vapor (H_2O) and oxygen (O_2). Decreases of TOA reflectance by the presence of smoke aerosols are indicated by dotted curves. (For interpretation of the references to color in this figure legend, the reader is referred to the web version of this article.)

In addition, the Monte Carlo method is also used to estimate the retrieval error in the smoke refractive index (Section 5). With the retrieval uncertainty of refractive index's PC weighting coefficients, we seed perturbated weighting coefficients, reconstruct the refractive index spectra, and assess the retrieval uncertainty in smoke refractive index.

3. Simulated TOA reflectance and observation error covariance

To investigate the impact of absorbing smoke aerosols residing on water cloud, we plot in Fig. 4 the spectra of TOA reflectance simulated for two ACA loadings (solid lines, $\tau^a_{550} = 0.5$ in blue and $\tau^a_{550} = 1.0$ in red), compared with a cloud-only (black) case using the optical properties summarized in Table 2. The spectral discontinuities result from strong absorption by trace gases, such as water vapor (H_2O at 0.72, 0.82, 0.94, 1.1, 1.35, 1.87, and 2.7–3.2 µm) and oxygen (O_2 at 0.68 and 0.76 µm and O_2–N_2 collision-induced absorption at 1.26 µm). In the absence of smoke, the TOA reflectance of the cloud scene decreases from UV to red spectral regions, caused by spectrally-dependent scattering of light by air molecules known as Rayleigh scattering. Cloud reflectance remains flat in the atmospheric windows between 600 and 1200 nm and decreases as wavelength increases. This can be explained by the flat scattering of cloud droplets in visible and NIR spectral regions along with the increasingly absorption at SWIR and MWIR wavelengths (Fig. 1c and d). Not surprisingly, the presence of smoke over the cloud deck results in a reduction of TOA reflectance that linearly depends on smoke burden. Due to the spectral variation of smoke AAOD (Fig. 2d), such reduction is more significant in shorter wavelengths, leading to a distinct spectral contrast.

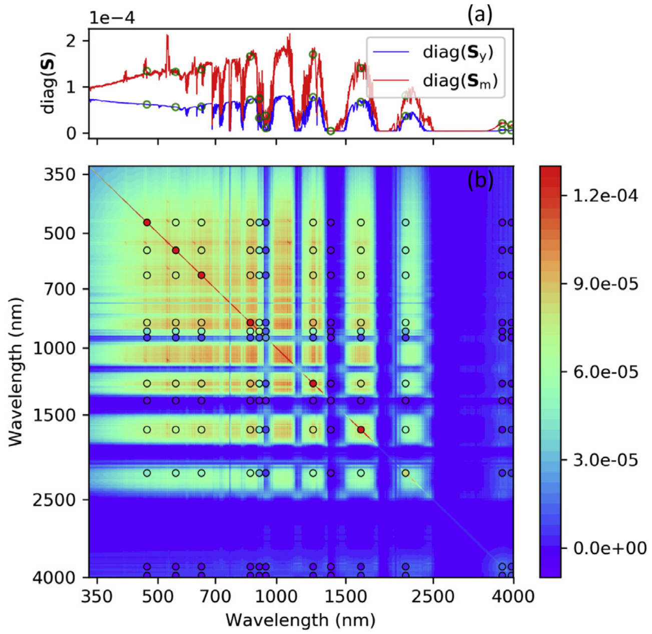

Fig. 5. Illustration of observation error covariance matrix. (a) Diagonal elements of instrumental and modeling error covariance matrices, diag(S_y) and diag(S_m), with a units of squared reflectance. (b) Graphics of observation error covariance matrix S_ϵ, where $S_\epsilon = S_y + S_m$. Circles indicate the S_ϵ of MODIS-type observations.

We characterize the observation error covariance matrix ($\mathbf{S}_\epsilon$) following the approach presented in 2.7. $\mathbf{S}_\epsilon$ are calculated by taking into account the instrument noises ($\mathbf{S}_y$) and forward model errors ($\mathbf{S}_m$) in the hyperspectral synthetic TOA reflectance. Fig. 5a illustrates the diagonal elements of $\mathbf{S}_y$ and $\mathbf{S}_m$, and their sum ($\mathbf{S}_\epsilon$) is shown in Fig. 5b. Circles indicate the $\mathbf{S}_\epsilon$ of MODIS-type observations. Whereas the diagonals are error variances of the observations, off-diagonals represent the error correlations between observations, mainly characterized by the model error covariance matrix $\mathbf{S}_m$. The low gaps in the error covariance correspond to gas-absorbing bands, where the errors of TOA reflectance are negligibly affected by other spectral bands.

4. Sensitivity of TOA spectral signature to cloud and aerosol properties

Along with the calculation of TOA reflectance, UNL-VRTM also computes the Jacobians of TOA reflectance with respect to cloud and ACA variables (or the Jacobian matrix $\mathbf{K}$) that serve as a sensitivity metric to depict their spectral signatures. In this section, we compare ϵ $(= [\mathrm{diag}(\mathbf{S}_\epsilon)]^{\frac{1}{2}})$ and $\tilde{\epsilon}$ $(= \mathbf{K}\,\mathbf{S}_a^{\frac{1}{2}})$ to better analyze the spectral signature of each retrieved variable. Here, ϵ represents observation error; $\tilde{\epsilon}$ is the Jacobian matrix normalized by prior errors in Table 2, thus representing the natural variability of observation as expressed by the prior uncertainty [69]. Any component whose natural variability is smaller than the observation error is not measurable. In other words, at any spectrum if the magnitude of the error-normalized Jacobian $\tilde{\epsilon}$ to a given parameter is less than the magnitude of ϵ, the TOA reflectance at this spectrum does not contain useful information for determining this parameter. Conversely, useful information is found if the former is larger than the latter, and the larger of the magnitude of $\tilde{\epsilon}$, the more useful information contained in the observation for the parameter. Therefore, comparison of $\tilde{\epsilon}$ and ϵ provides not only sensitivity of individual measurements to each retrieved parameter but also a capacity metric for those observations to infer that parameter.

4.1. Sensitivity to cloud properties

Fig. 6a–c shows the components of $\tilde{\epsilon}$ for cloud droplet properties under two different smoke loadings ($\tau^a_{550} = 0.5$ in blue and $\tau^a_{550} = 1.0$ in red). The filled grey color indicates the domain of $\pm[\mathrm{diag}(\mathbf{S}_\epsilon)]^{\frac{1}{2}}$, i.e. the range of observation error ϵ. Clearly, the lofted smoke dims the sensitivity of TOA reflectance to cloud in the shorter wavelengths where smoke is optically significant (red versus blue curves), while the TOA reflectance could be increased by thickened cloud optical loading, reduced effective droplet size, or widened dispersion of droplet size. Also, the magnitudes of $\tilde{\epsilon}$ for COD and r^c_{eff} are significantly outbound the observation error, and these sensitivities vary differently along spectral wavelength. For instance, sensitivities to both COD and droplet effective radius (r^c_{eff}) grow with the increase of wavelength from UV to NIR (Fig. 6a and b). At the same time, the former gradually diminishes but the later remains strong in the shortwave IR. In contrast, the $\tilde{\epsilon}$ for v^c_{eff} remains weak until the spectral wavelength exceeds 1500 nm (Fig. 6c). Therefore, TOA reflectance at wavelengths shorter than 1500 nm provide information for both COD and droplet size, longer wavelengths provide information primarily on droplet sizes. This fact has been used to retrieve r^c_{eff} and COD from satellite instruments, such as the AVHRR and MODIS [e.g., 23,31,45].

4.2. Sensitivity to smoke properties

In contrast to cloud, the above-cloud smoke particles act distinctively on the TOA reflectance. Fig. 6d–f shows error normalized Jacobians of TOA reflectance to smoke 550-nm AOD, r^a_{eff}, and v^a_{eff}, displaying overall negative sensitivities for all of these three variables. Furthermore, the more abundant of smoke aerosols, the stronger the sensitivities are. In particular, TOA reflectance in UV–visible provide information primarily on ACA AOD (Fig. 6d), and at intermediate wavelengths in visible-NIR provide information on both AOD and r^a_{eff} (Fig. 6d and e). In fact, the information peaks at wavelengths around 750 nm for r^a_{eff}. In contrast, TOA reflectance at wavelengths greater than 2000 nm almost do not respond to smoke variables, as smoke is transparent for light in SWIR. However, the magnitudes of the $\tilde{\epsilon}$ for v^a_{eff} are lower than observation error at the entire spectral range (Fig. 6f), even though TOA reflectance is sensitive to v^a_{eff} to some extent around 1000 nm.

Fig. 6g plots the error-normalized Jacobian of TOA reflectance to cloud-aerosol separation H. We can see that radiances at UV and blue wavelengths reduce significantly as aerosol smoke layer increases, because an elevated smoke layer absorbs solar radiation and reduces the chance of the light being scattered by underlying clouds and air molecules [57]. As such, the magnitude of this Jacobian reduces along with the weakening of Rayleigh scattering or the increase of wavelengths. Indeed, the UV absorbing aerosol index, which represents the enhancement of spectral contrast in UV by aerosol absorption, were found substantially sensitive to H [14,58]. In addition, the signature for H is enhanced by absorptions of O_2 and H_2O (vapor) at wavelengths between 680 and 1500 nm. While smoke aerosols absorb sunlight, they also scatter light back to space and reduce the chance of light being absorbed by underlying water vapor and O_2. Therefore, the higher of the smoke layer, the stronger the reflected radiative signals received by satellite; this principle has been used by many studies to derive layer height of aerosol and cloud from satellite measurements in the O_2 or H_2O absorption bands [e.g., 67,70].

Fig. 7a and e, similar to Fig. 6, present the error-normalized sensitivities of TOA reflectance to the complex refractive index of smoke. Real and imaginary parts of refractive index describe smoke's scattering and absorption properties, respectively. The sensitivity of radiance to smoke absorption primarily occurs in UV and visible regions and decreases with wavelength (Fig. 7e). In contrast,

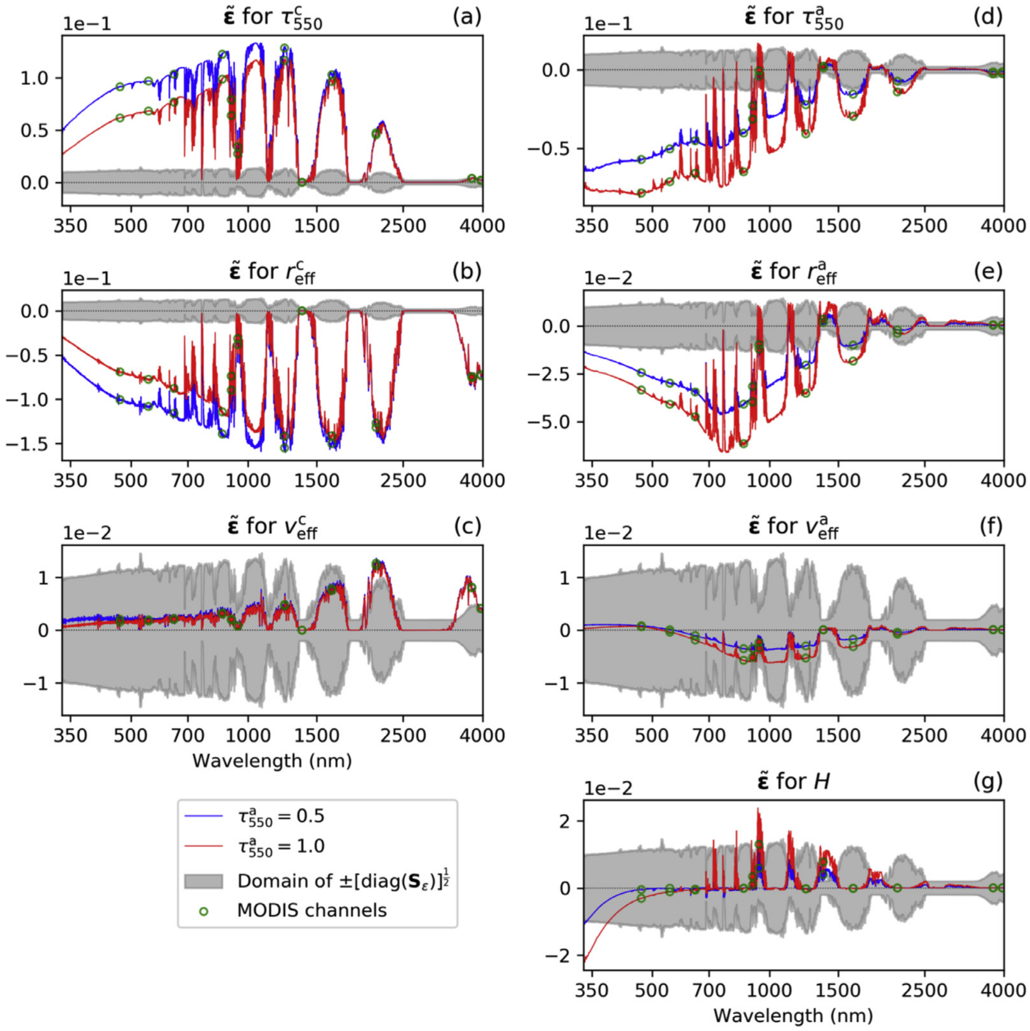

Fig. 6. Error-normalized Jacobians ($\tilde{\epsilon}$) of TOA reflectance with respect to smoke and cloud physical variables. Each panel corresponds to Jacobians with respect to one variable, i.e., (a) τ^{c}_{550}, (b) r^{c}_{eff}, (c) v^{c}_{eff}, (d) τ^{a}_{550}, (e) r^{a}_{eff}, (f) v^{a}_{eff}, and (g) H. These Jacobians are calculated by UNL-VRTM under two smoke loadings: 550-nm AOD of 0.5 (blue) and 1.0 (red). The filled grey color indicates the range of observation error ϵ. Circles indicate spectral bands of MODIS-type observations. (For interpretation of the references to color in this figure legend, the reader is referred to the web version of this article.)

the information to real part of smoke refractive index peaks at wavelengths around 700–800 nm, decreasing for longer or shorter wavelengths (Fig. 7a). Additionally, while sensitivity to smoke absorption doubles for a twofold increase in smoke loading, the sensitivity to real part of refractive index decreases in UV and visible regions.

Following Eqs. (9 and 10), we calculated Jacobian gradient of TOA reflectance with respect to PC weighting coefficients of the smoke refractive index spectra. The $\tilde{\epsilon}$ for PC coefficients of real and imaginary parts are shown in Fig. 7b and d and f and h, respectively. Indeed, these Jacobians are determined by Eq. (10) using the PCs of smoke refractive index (Fig. 3a and b) and Jacobians of TOA reflectance to refractive index (Fig. 7a and e). The sensitivities for $w_{r,\ 1}$ and $w_{i,\ 1}$ have similar spectral variability to those for m^{a}_{r} and m^{a}_{i}, since the 1st PC accounts for the largest possible variance of original variables. In contrast, sensitivities for the succeeding PC coefficients exhibit smaller-scale spectral variations. Comparatively, TOA reflectance contains more information for m_{i} than that for m_{r}, as the magnitudes of $\tilde{\epsilon}$ is larger than ϵ for m^{a}_{i} but smaller for m^{a}_{r}.

5. Information content and retrieval error

Based on observation error covariance and Jacobian matrix presented in preceding sections, we calculated averaging kernel matrix $\mathbf{A}$ and posterior error covariance matrix $\hat{\mathbf{S}}$ for both the hyperspectral and MODIS-type observation scenarios at $\tau^{a}_{550} = 0.5$. We then derived the total and partial DFS, as well as the expected error of each retrieved variable. For each observation scenario, we consider two different spectral settings: (A) 400–2400 nm, and (B) 333–4000 nm. Spectral setting B represents the full solar spectral range. In contrast, setting A does not include UV and MWIR, which is similar to the spectral range of AVIRIS-NG instrument. Here we include analysis for spectral setting A by also considering the fact that Raman scattering in UV and thermal component in MWIR can bring complexity in radiative transfer simulation. For instance, thermal component in the MWIR channels around 3.7 µm is significant and has to be removed to obtain the reflected solar signal [46].

Fig. 8 illustrates partial DFS (top) and the ratio of retrieval error to priori error (bottom) of each state parameter. Retrieval error of each parameter is also listed in Table 3. Hyperspectral and MODIS-

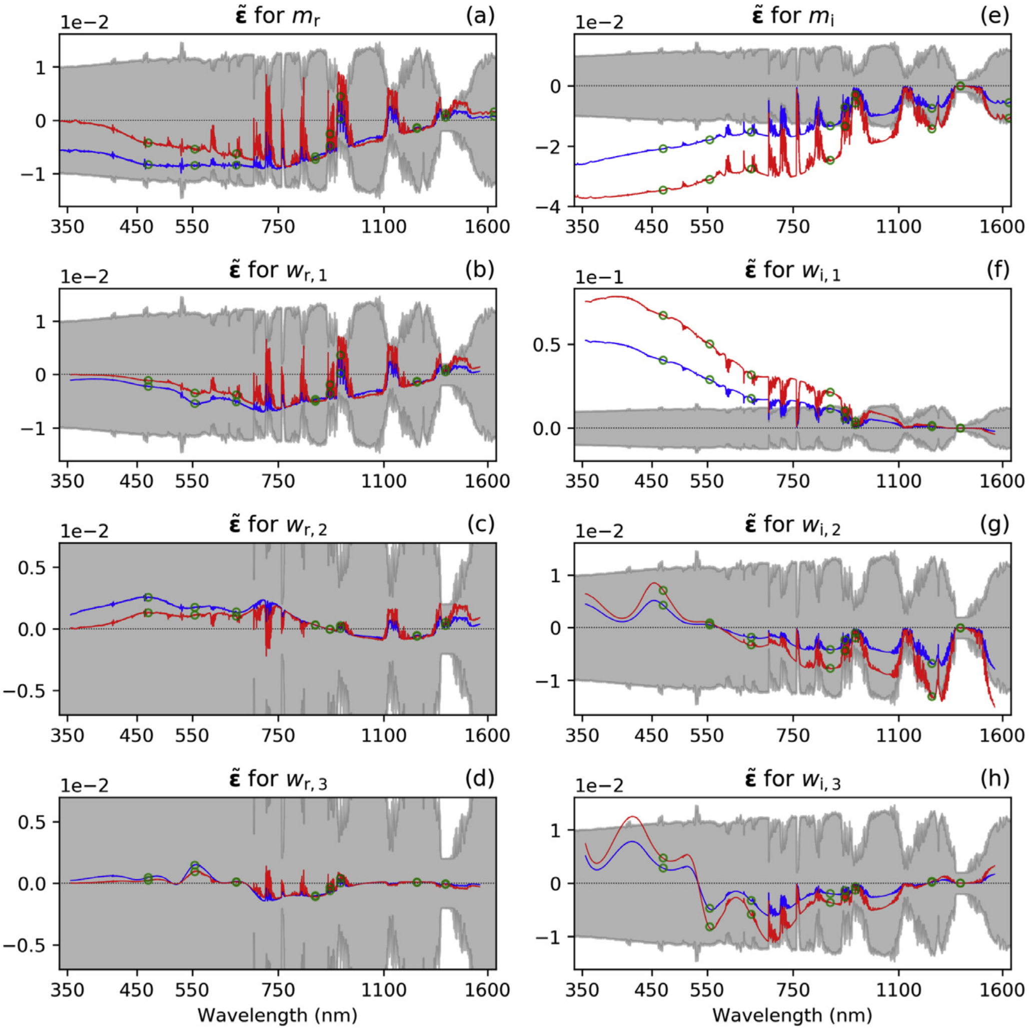

Fig. 7. Same to Fig. 6, but for error-normalized Jacobians ($\tilde{\epsilon}$) of TOA reflectance with respect to (a) m_r^a and (e) m_i^a, as well as their first 3 PC weighting coefficients (b-d and f-h). Figure legend can also be found in Fig. 6.

Table 3
Posterior errors ($\hat{\epsilon}$) of retrieved parameters from hyperspectral (Hyper) and MODIS-type observations for the case of $\tau_{550}^a = 0.5$.

	Cloud parameters			Smoke parameters				PC weights of refractive index					
	τ_{550}^c	r_{eff}^c (μm)	ν_{eff}^c	H(km)	τ_{550}^a	r_{eff}^a (μm)	ν_{eff}^a	$w_{\mathrm{r},1}$	$w_{\mathrm{r},2}$	$w_{\mathrm{r},3}$	$w_{\mathrm{i},1}$	$w_{\mathrm{i},2}$	$w_{\mathrm{i},3}$
Hyper A	0.41	0.39	0.02	0.44	0.09	0.02	0.09	2.43	1.20	0.42	0.14	0.07	0.03
Hyper B	0.36	0.24	0.02	0.38	0.04	0.01	0.09	2.16	1.12	0.39	0.03	0.07	0.02
MODIS A	1.07	0.65	0.05	1.71	0.18	0.04	0.10	3.30	1.46	0.49	0.35	0.16	0.07
MODIS B	0.65	0.30	0.04	1.71	0.17	0.04	0.10	3.30	1.46	0.49	0.35	0.16	0.06

like observation scenarios are referred to “Hyper A” and “MODIS A” for spectral range setting of 400–2400 nm, and “Hyper B” and “MODIS B” for the setting of 333–4000 nm. Overall, we found a total DFS of 10.0 for Hyper-B measurements, which represents an increase of about 5 from that of MODIS-B measurements. In other words, SW hyperspectral measurements contain more information that can be used to retrieve about 5 more parameters. The same amount of increased information is also found for observations in 400–2400 nm.

According to Fig. 8a, MODIS-A and MODIS-B observations can yield 4.5 and 4.8 pieces of information, respectively. The difference of 0.3 DFS comes from the information for ν_{eff}^c gained for MODIS-B measurements, as TOA reflectance in SWIR contains partial information for ν_{eff}^c (Fig. 6c). In general, information from MODIS-type observations are distributed primarily amongst the COD, r_{eff}^c, ACA AOD, and r_{eff}^a. Retrieval uncertainties in these variables are 0.65, 0.30 µm, 0.17, and 0.04 µm, respectively, which represent 13%, 6%, 43%, and 33% of their prior uncertainties. However, MODIS-type observation has difficulty to resolve H, ν_{eff}^c, ν_{eff}^a, and smoke refractive index. We note the uncertainty in retrieving ACA AOD is 0.17, or a relative error of 43%. This magnitude is consistent with the estimated uncertainties (−10% to 50%) of ACA AOD retrieved by the MODIS “color ratio” algorithms [28,29].

In comparison, hyperspectral observations (for both the spectral settings of A and B) can significantly advance the retrieval accuracy of these four parameters. Specifically, in the hyperspectral scenarios the uncertainties in retrieved COD, r_{eff}^c, AOD, and r_{eff}^a are 0.36, 0.25 µm, 0.04, and 0.01 µm, respectively. Not just improving the retrieval uncertainty in these parameters, hyperspectral observations also offer additional information to retrieve H, ν_{eff}^c, and smoke re-

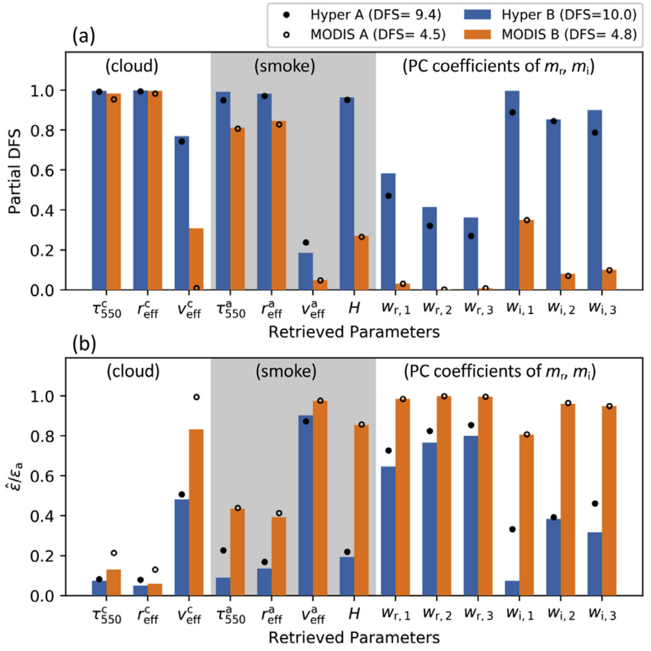

Fig. 8. Information content of hyperspectral (Hyper) and MODIS-type observations and resulting retrieval uncertainty for each cloud and smoke variable for the case of $\tau^a_{550} = 0.5$. Two spectral settings are corresponding to spectral range of 400–2400 nm (Hyper A and MODIS A) and 333–4000 nm (Hyper B and MODIS B), respectively. (a) Partial DFS values for each retrieved variable. (b) Ratio of retrieval error to prior error ($\widehat{\epsilon}/\epsilon_a$) of each variable.

fractive index. For instance, partial DFS for v^c_{eff} reaches 0.77, leading to a retrieval error of about 0.024, which represent 48% of its prior error. The retrieval accuracy for H is about 0.4 km. Similarly, retrieval errors of PC coefficients ($\mathbf{w}$) for complex refractive index spectra also see substantial reductions from their prior uncertainties. The reductions are more notable for $\mathbf{w}_i$, indicating aerosol absorption can be well retrieved from hyperspectral measurements. However, hyperspectral data have no information for improving the retrievals of v^a_{eff} and only limited information for retrieving the real part of refractive index.

To illustrate the capability for retrieving smoke refractive index, we propagate the retrieval error from $\mathbf{w}$ to the refractive index spectra using the Monte Carlo approach. The process is the same approach as that used to characterize observation error in Section 2.7. Here, we first reconstruct refractive index spectra using normally-distributed random samplings of $\mathbf{w}$ within the range of its given error. Then, the retrieval errors of refractive index are characterized by ensemble variance of those reconstructed spectra: A smaller variance indicates a more accurate retrieval. Specifically, we reconstructed three ensembles of refractive index spectra based on three ensembles of $\mathbf{w}$ that were sampled according to the prior error, and retrieval error from MODIS-B and Hyper-B measurements, respectively. Fig. 9a and b illustrates the ranges of these ensembles for m^a_r and m^a_i spectra, and Fig. 9c and d presents their standard deviations. The ensemble based on prior errors (light blue color) represents variability of the refractive indices adopted for PCA, namely, the Magi07 database. Similarly, the ensembles based on hyperspectral (blue) and MODIS-type (orange) inversions can describe their retrieval accuracy in m^a_r and m^a_i. We can see that (1) MODIS-type observations yield some information to m^a_i in the visible wavelengths but almost no information to m^a_r; (2) Hyperspectral observations can offer an abundant amount of information to retrieve m^a_i but only a moderate amount of information to retrieve m^a_r. Therefore, we can conclude that hyperspectral measurements are a valuable for accurately retrieving the spectral absorption of the above-cloud smoke aerosols.

6. Conclusions

We conducted an observation simulation experiment to investigate the potential for simultaneously retrieving properties of above-cloud aerosols (ACA) and underlying liquid clouds from shortwave hyperspectral measurements over an ocean surface. Our study focuses on a state vector that consists of cloud optical depth (COD) at 550 nm, droplet effective radius (r^c_{eff}) and effective variance (v^c_{eff}), aerosol-cloud relative altitude (H), aerosol optical depth (AOD) at 550 nm, particle effective radius (r^a_{eff}) and effective variance (v^a_{eff}), and complex aerosol refractive index (m^a_r and m^a_i.) represented by weighting coefficients ($\mathbf{w}_r$ and $\mathbf{w}_r$) of principal components (PCs). The experiment first generates synthetic TOA reflectance in 330–4000 nm for typical ACA scenarios. Next, the observation error covariance matrix is characterized to account for instrumental noise and model errors. Then, the spectral signatures of cloud and ACA are analyzed with the error-normalized Jacobian gradients of TOA reflectance with respect to the state vector. Lastly, information content of the synthetic data is assessed in terms of the degree of freedom for signals (DFS), and the retrieval uncertainty of each variable in the state vector are estimated. In order to highlight the advantage of hyperspectral inversion, we compare information contents offered by hyperspectral data with those by the MODIS-type multi-spectral data. In brief, our findings can be summarized as

1. The presence of smoke over the cloud deck results in a reduction of TOA reflectance that is relatively more significant in shorter wavelength due to the spectral variation of smoke AAOD.
2. While TOA reflectance is sensitive to most elements in the state vector, the spectral variability of such sensitivity is different from one element to another. In other words, the spectral variation in TOA reflectance due to each cloud and ACA variable is different.
3. MODIS, which has limited spectral bands in the solar spectrum, only has sufficient information for reliably retrieving COD and r^c_{eff} and partial information for retrieving smoke AOD and r^a_{eff}. In contrast, hyperspectral measurements have 5 extra pieces of information (double in terms of DFS compared to MODIS), allowing the retrieval of additional aerosol and cloud microphysical parameters, i.e., effective variance of droplet size, smoke refractive indices, and H. Specifically, estimated uncertainties in the MODIS inversion of COD, r^c_{eff}, AOD, r^a_{eff} are 0.65, 0.30 µm, 0.17, and 0.04 µm, respectively. In contrast, the counterparts in the hyperspectral inversion are 0.36, 0.25 µm, 0.04, and 0.01 µm, respectively. Hyperspectral inversion can also provide H and $v^c_{eff}$with estimated uncertainties of 0.4 km and 0.2, respectively, together with constrained m^a_i for accurately characterizing aerosol absorption. Therefore, hyperspectral inversion can provide strong constraints on quantifying the heating rate of absorbing aerosols above clouds.

In our analysis we use a spectral resolution and sampling of 5 cm^{-1} wavelength number in the spectral range of 333–4000 nm. The information content and error characterization thus represent what can be achieved with a spectrometer of such an ideal spectral configuration. In practice, the same approach can be applied to measurements of any specific instruments, such as the TROPOMI [60], the shortwave spectrometer for Climate Absolute Radiance and Refractivity Observatory (CLARREO) mission [63], the 4STAR instrument [51], or the collocated Ozone Monitoring Instrument (OMI) and MODIS data. Our future efforts will focus on developing the retrieval algorithm for a specific spectrometer (such as 4STAR)

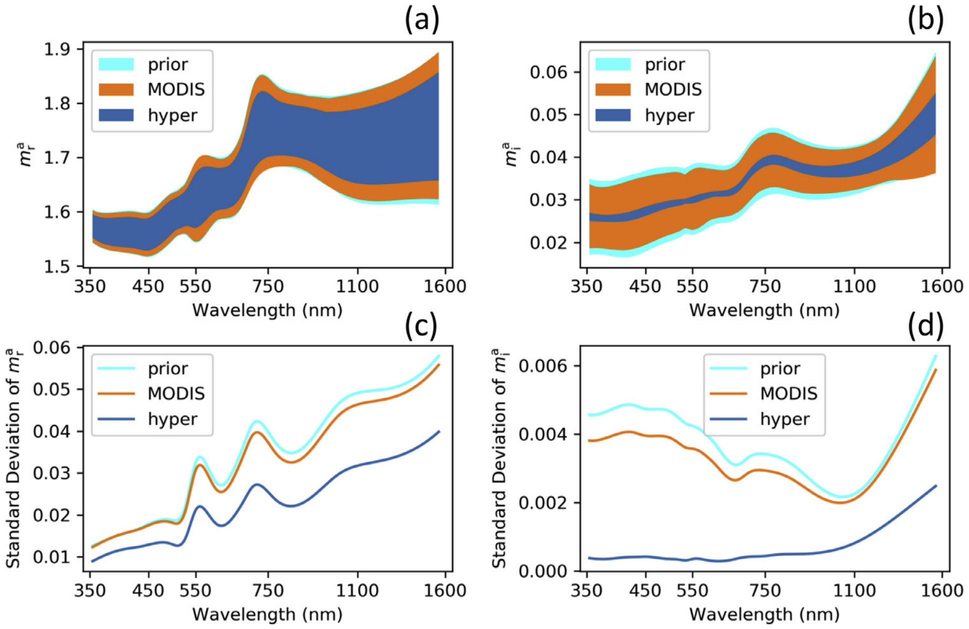

Fig. 9. Uncertainties in the PC-reconstructed refractive index spectra. (a-b) Ranges of reconstructed m_r^a and m_i^a spectra characterized by prior error (light blue), retrieval error from MODIS-B observations (orange), and retrieval error from Hyper-B observations (blue). (c-d) Same as panels (a-b) but for standard deviation of reconstructed m_r^a and m_i^a spectra. (For interpretation of the references to color in this figure legend, the reader is referred to the web version of this article.)

and conducting retrievals of ACA and underlying cloud properties using real measurements. In addition, it has been noted that multi-angular polarimetric measurements also contain valuable information for retrieving ACA properties [32,62,68]. A further investigation of angular spectro-polarimetric measurements for ACA retrievals would be an interesting subsequent study.

Finally, it should be noted that this study is purely based on modeling simulations. The results and conclusions thus depend on the assumptions made in the radiative transfer simulation and the OE information analysis, including idealized instrument error characteristics that in practice are difficult to quantify. In reality, the algorithm development would face challenges to address more complicated situations. For instance, we calculate smoke optical properties by assuming that smoke particles are spheres following a mono-mode lognormal size distribution. Whereas, soot smoke particles are often structured as fractal-like chain aggregates [10,41]. Studies have shown Mie scattering, which cannot address the complex morphology of soot, can have profound bias on scattering and absorption properties [6,34,47]. However, smoke morphology changes with aging during transport and its characterization remains highly uncertain [73]. It is difficult to examine how smoke morphology impacts the results and conclusions in this study. Another limitation is that this study focuses on remote sensing over ocean and thus restricts its application over land surface. In contrast to water, the land surface reflectance has large spectral and spatial changes. While the impact from land surface would be large for optically thin clouds, the impact is negligible for thick clouds, because the opacity of clouds prevents the light from penetrating to the underlying surface. Additionally, the OE inversion technique with hyper-spectral radiative transfer simulation has a computational challenge. A further study on spectral selection is needed to reduce the computation cost. Indeed, many spectral bands contain little useful information (Figs. 6 and 7). In practical implementation, one can choose a limited number of bands that are most informative for retrieval [e.g., [17,26]]. Hence, the results presented in this paper should be viewed as a back-of-the-envelope analysis of cloud and smoke information content in (hypothetical) hyperspectral measurements. For any specific instrument, the instrument errors (such as from cross-band talk and calibration) need to be further characterized before they can be fully considered in the information content analysis.

Acknowledgments

This research is in part supported by National Aeronautics and Space Administration under grant NNX17AF78G issued through the Atmospheric Composition Spectral Climate Signal Programmanaged by Hal Maring, grant NNX17AF77G issued through ACMAP program managed by Richard Eckman, and through Terra/Aqua/S-NPP program (grant number 80NSSC18K0846). It is in part supported by Office of Naval Research (ONR’s) Multidisciplinary University Research Initiatives (MURI) Program under the award No. N00014-16-1-2040. We acknowledge the computational support from the High Performance Computing group at The University of Iowa. We are grateful for the inisightful discussion and comments from Dr. Feng Xu and three anonymous reviwers. The data presented in this paper can be obtained through email to the corresponding authors (X. Xu and J. Wang) of this paper.

Supplementary materials

Supplementary material associated with this article can be found, in the online version, at doi:10.1016/j.jqsrt.2018.09.024.

References

[1] Alfaro-Contreras R, Zhang J, Campbell JR, Holz RE, Reid JS. Evaluating the impact of aerosol particles above cloud on cloud optical depth retrievals from MODIS. J Geophys Res 2014;119(9):5410–23. doi:10.1002/2013JD021270.

[2] Alfaro-Contreras R, Zhang J, Campbell JR, Reid JS. Investigating the frequency and interannual variability in global above-cloud aerosol characteristics with CALIOP and OMI. Atmos Chem Phys 2016;16(1):47–69. doi:10.5194/acp-16-47-2016.

[3] Baldridge AM, Hook SJ, Grove CI, Rivera G. The ASTER spectral library version 2.0. Remote Sens Environ 2009;113(4):711–15. doi:10.1016/j.rse.2008.11.007.

[4] Bodhaine BA, Wood NB, Dutton EG, Slusser JR. On Rayleigh optical depth calculations. J Atmos Ocean Technol 1999;16(11):1854–61. doi: 10.1175/1520-0426(1999)016⟨1854:ORODC⟩2.0.CO;2.

[5] Borovikov A, Rienecker MM, Keppenne CL, Johnson GC. Multivariate error covariance estimates by Monte Carlo simulation for assimilation studies in

the Pacific Ocean. Month Weather Rev 2005;133(8):2310–34. doi:10.1175/mwr2984.1.

[6] Chakrabarty RK, Moosmüller H, Arnott WP, Garro MA, Slowik JG, Cross ES, Han J-H, Davidovits P, Onasch TB, Worsnop DR. Light scattering and absorption by fractal-like carbonaceous chain aggregates: comparison of theories and experiment. Appl Opt 2007;46(28):6990–7006. doi:10.1364/AO.46.006990.

[7] Chand D, Wood R, Anderson TL, Satheesh SK, Charlson RJ. Satellite-derived direct radiative effect of aerosols dependent on cloud cover. Nat Geosci 2009;2(3):181–4. doi:10.1038/ngeo437.

[8] Chang I, Christopher SA. The impact of seasonalities on direct radiative effects and radiative heating rates of absorbing aerosols above clouds. Q J R Meteorol Soc 2017:1395–405. doi:10.1002/qj.3012.

[9] Chen X, Wang J, Liu Y, Xu X, Cai Z, Yang D, Yan C-X, Feng L. Angular dependence of aerosol information content in CAPI/TanSat observation over land: effect of polarization and synergy with A-train satellites. Remote Sens Environ 2017;196:163–77. doi:10.1016/j.rse.2017.05.007.

[10] China S, et al. Morphology and mixing state of aged soot particles at a remote marine free troposphere site: implications for optical properties. Geophys Res Lett 2015;42(4):1243–50. doi:10.1002/2014GL062404.

[11] Clough SA, Kneizys FX, Davies RW. Line shape and the water vapor continuum. Atmos Res 1989;23(3):229–41. doi:10.1016/0169-8095(89)90020-3.

[12] Das S, Harshvardhan H, Bian H, Chin M, Curci G, Protonotariou AP, Mielonen T, Zhang K, Wang H, Liu X. Biomass burning aerosol transport and vertical distribution over the South African–Atlantic region. J Geophys Res 2017;122(12):6391–415. doi:10.1002/2016JD026421.

[13] Davis A, Marshak A, Cahalan R, Wiscombe W. The landsat scale break in stratocumulus as a three-dimensional radiative transfer effect: implications for cloud remote sensing. J Atmos Sci 1997;54(2):241–60. doi: 10.1175/1520-0469(1997)054⟨0241:Tlsbis⟩2.0.Co;2.

[14] de Graaf M, Stammes P, Torres O, Koelemeijer RBA. Absorbing aerosol index: sensitivity analysis, application to GOME and comparison with TOMS. J Geophys Res 2005;110(D1). doi:10.1029/2004JD005178.

[15] de Graaf M, Tilstra LG, Wang P, Stammes P. Retrieval of the aerosol direct radiative effect over clouds from spaceborne spectrometry. J Geophys Res 2012;117:D07207. doi:10.1029/2011jd017160.

[16] Devasthale A, TjernstrÖM M, Omar AH. The vertical distribution of thin features over the Arctic analysed from CALIPSO observations. Tellus B 2011;63(1):86–95. doi:10.1111/j.1600-0889.2010.00517.x.

[17] Ding S, Wang J, Xu X. Polarimetric remote sensing in oxygen A and B bands: sensitivity study and information content analysis for vertical profile of aerosols. Atmos Meas Technol 2016;9(5):2077–92. doi:10.5194/amt-9-2077-2016.

[18] Downing HD, Williams D. Optical constants of water in the infrared. J Geophys Res 1975;80(12):1656–61. doi:10.1029/JC080i012p01656.

[19] Dubovik O, Holben B, Eck TF, Smirnov A, Kaufman YJ, King MD, Tanr√© D, Slutsker I. Variability of absorption and optical properties of key aerosol types observed in worldwide locations. J Atmos Sci 2002;59(3):590–608. doi: 10.1175/1520-0469(2002)059⟨0590:voaaop⟩2.0.co;2.

[20] Feng N, Christopher SA. Measurement-based estimates of direct radiative effects of absorbing aerosols above clouds. J Geophys Res 2015;120(14):6908–21. doi:10.1002/2015JD023252.

[21] Ge C, Wang J, Reid JS. Mesoscale modeling of smoke transport over the Southeast Asian Maritime Continent: coupling of smoke direct radiative effect below and above the low-level clouds. Atmos Chem Phys 2014;14(1):159–74. doi:10.5194/acp-14-159-2014.

[22] Hale GM, Querry MR. Optical constants of water in the 200-nm to 200-µm wavelength region. Appl Opt 1973;12(3):555–63. doi:10.1364/AO.12.000555.

[23] Han Q, Rossow WB, Lacis AA. Near-global survey of effective droplet radii in liquid water clouds using ISCCP data. J Clim 1994;7(4):465–97. doi: 10.1175/1520-0442(1994)007⟨0465:Ngsoed⟨2.0.Co;2.

[24] Hansen JE, Travis LD. Light scattering in planetary atmospheres. Space Sci Rev 1974;16:572–610.

[25] Haywood JM, Osborne SR, Abel SJ. The effect of overlying absorbing aerosol layers on remote sensing retrievals of cloud effective radius and cloud optical depth. Q J R Meteorol Soc 2004;130(598):779–800. doi:10.1256/qj.03.100.

[26] Hou W, Wang J, Xu X, Reid JS. An algorithm for hyperspectral remote sensing of aerosols: 2. Information content analysis for aerosol parameters and principal components of surface spectra. J Quant Spectrosc Radiat Transf 2017;192:14–29. doi:10.1016/j.jqsrt.2017.01.041.

[27] Hou W, Wang J, Xu X, Reid JS, Han D. An algorithm for hyperspectral remote sensing of aerosols: 1. Development of theoretical framework. J Quant Spectrosc Radiat Transf 2016;178:400–15. doi:10.1016/j.jqsrt.2016.01.019.

[28] Jethva H, Torres O, Remer L, Bhartia PK. A color ratio method for simultaneous retrieval of aerosol and cloud optical thickness of above-cloud absorbing aerosols from passive sensors: application to MODIS measurements. IEEE Trans Geosci Remote Sens 2013;51(7):3862–70. doi:10.1109/TGRS.2012.2230008.

[29] Jethva H, Torres O, Remer L, Redemann J, Livingston J, Dunagan S, Shinozuka Y, Kacenelenbogen M, Rosenheimer MS, Spurr R. Validating MODIS above-cloud aerosol optical depth retrieved from "color ratio" algorithm using direct measurements made by NASA's airborne AATS and 4STAR sensors. Atmos Meas Technol, 2016;9(10):5053–62. doi:10.5194/amt-9-5053-2016.

[30] Johnson BT, Shine KP, Forster PM. The semi-direct aerosol effect: Impact of absorbing aerosols on marine stratocumulus. Q J R Meteorol Soc 2004;130(599):1407–22. doi:10.1256/qj.03.61.

[31] King MD, Menzel WP, Kaufman YJ, Tanre D, Bo-Cai G, Platnick S, Ackerman SA, Remer LA, Pincus R, Hubanks PA. Cloud and aerosol properties, precipitable water, and profiles of temperature and water vapor from MODIS. IEEE Trans Geosci Remote Sens 2003;41(2):442–58. doi:10.1109/TGRS.2002.808226.

[32] Kokhanovsky AA, et al. Space-based remote sensing of atmospheric aerosols: the multi-angle spectro-polarimetric frontier. Earth-Sci Rev 2015;145:85–116. http://dx.doi.org/10.1016/j.earscirev.2015.01.012.

[33] Kou L, Labrie D, Chylek P. Refractive indices of water and ice in the 0.65 to 2.5-µm spectral range. Appl Opt 1993;32(19):3531–40. doi:10.1364/AO.32.003531.

[34] Liu L, Mishchenko MI, Patrick Arnott W. A study of radiative properties of fractal soot aggregates using the superposition T-matrix method. J Quant Spectrosc Radiat Transf 2008;109(15):2656–63. https://doi.org/10.1016/j.jqsrt.2008.05.001.

[35] Magi BI, Fu Q, Redemann J. A methodology to retrieve self-consistent aerosol optical properties using common aircraft measurements. J Geophys Res 2007;112(D24):D24S12. doi:10.1029/2006JD008312.

[36] McClatchey RA, Fenn RW, Selby JEA, Volz FE, Garing JS. Optical properties of the atmosphere. Hanscom AFB, MA: Air Force Cambridge Research Labs; 1972. p. 110.

[37] Meyer K, Platnick S, Oreopoulos L, Lee D. Estimating the direct radiative effect of absorbing aerosols overlying marine boundary layer clouds in the southeast Atlantic using MODIS and CALIOP. J Geophys Res 2013;118(10):4801–15. doi:10.1002/jgrd.50449.

[38] Meyer K, Platnick S, Zhang Z. Simultaneously inferring above-cloud absorbing aerosol optical thickness and underlying liquid phase cloud optical and microphysical properties using MODIS. J Geophys Res 2015;120(11):5524–47. doi:10.1002/2015jd023128.

[39] Miles NL, Verlinde J, Clothiaux EE. Cloud droplet size distributions in low-level Stratiform clouds. J Atmos Sci 2000;57(2):295–311 doi:10.1175/1520-0469(2000)057<0295:Cdsdil>2.0.Co;2.

[40] Mlawer EJ, Payne VH, Moncet J-L, Delamere JS, Alvarado MJ, Tobin DC. Development and recent evaluation of the MT_CKD model of continuum absorption. Philos Trans R Soc A 2012;370:2520–56. doi:10.1098/rsta.2011.0295.

[41] Moosmüller H, Chakrabarty RK, Arnott WP. Aerosol light absorption and its measurement: a review. J Quant Spectrosc Radiat Transf 2009;110(11):844–78. https://doi.org/10.1016/j.jqsrt.2009.02.035.

[42] Myhre G, et al. Radiative forcing of the direct aerosol effect from AeroCom Phase II simulations. Atmos Chem Phys 2013;13(4):1853–77. doi:10.5194/acp-13-1853-2013.

[43] Nakajima T, King MD, Spinhirne JD, Radke LF. Determination of the optical thickness and effective particle radius of clouds from reflected solar radiation measurements. Part II: Marine stratocumulus observations. J Atmos Sci 1991;48(5):728–51 doi:10.1175/1520-0469(1991)048<0728:Dotota>2.0.Co;2.

[44] Peters K, Quaas J, Bellouin N. Effects of absorbing aerosols in cloudy skies: a satellite study over the Atlantic Ocean. Atmos Chem Phys 2011;11(4):1393–404. doi:10.5194/acp-11-1393-2011.

[45] Platnick S, King MD, Ackerman SA, Menzel WP, Baum BA, Riedi JC, Frey RA. The MODIS cloud products: algorithms and examples from Terra. IEEE Trans Geosci Remote Sens 2003;41(2):459–73. doi:10.1109/TGRS.2002.808301.

[46] Platnick S, Valero FPJ. A validation of a satellite cloud retrieval during ASTEX. J Atmos Sci 1995;52(16):2985–3001. doi: 10.1175/1520-0469(1995)052⟨2985:Avoasc⟩2.0.Co;2.

[47] Radney JG, You R, Ma X, Conny JM, Zachariah MR, Hodges JT, Zangmeister CD. Dependence of soot optical properties on particle morphology: measurements and model comparisons. Environ Sci Technol 2014;48(6):3169–76. doi:10.1021/es4041804.

[48] Rodgers CD. Inverse methods for atmospheric sounding: theory and practice. Singapore: World Scientific; 2000.

[49] Rothman LS, et al. The HITRAN2012 molecular spectroscopic database. J Quant Spectrosc Radiat Transf 2013;130:4–50. doi:10.1016/j.jqsrt.2013.07.002.

[50] Rothman LS, et al. The HITRAN 2008 molecular spectroscopic database. J Quant Spectrosc Radiat Transf 2009;110(9–10):533–72.

[51] Segal-Rosenheimer M, et al. Tracking elevated pollution layers with a newly developed hyperspectral Sun/Sky spectrometer (4STAR): results from the TCAP 2012 and 2013 campaigns. J Geophys Res 2014;119(5):2611–28. doi:10.1002/2013JD020884.

[52] Spurr R. A new approach to the retrieval of surface properties from earthshine measurements. J. Quant Spectrosc Radiat Transf 2004;83(1):15–46. doi:10.1016/S0022-4073(02)00283-2.

[53] Spurr R. VLIDORT: a linearized pseudo-spherical vector discrete ordinate radiative transfer code for forward model and retrieval studies in multilayer multiple scattering media. J Quant Spectrosc Radiat Transf 2006;102:316–42.

[54] Spurr R, Christi M. On the generation of atmospheric property Jacobians from the (V)LIDORT linearized radiative transfer models. J Quant Spectrosc Radiat Transf 2014;142(0):109–15. doi:10.1016/j.jqsrt.2014.03.011.

[55] Spurr R, Wang J, Zeng J, Mishchenko MI. Linearized T-matrix and Mie scattering computations. J Quant Spectrosc Radiat Transf 2012;113(6):425–39. doi:10.1016/j.jqsrt.2011.11.014.

[56] Xu X, Wang J, Wang Y, Henze DK, Zhang L, Grell GA, McKeen SA, Wielicki BA. Sense size-dependent dust loading and emission from space using reflected solar and infrared spectral measurements: An observation system simulation experiment. Journal of Geophysical Research: Atmospheres 2017;122. doi:10.1002/2017JD026677.

[57] Torres O, Bhartia PK, Herman JR, Ahmad Z, Gleason J. Derivation of aerosol properties from satellite measurements of backscattered ultraviolet radiation: theoretical basis. J Geophys Res 1998;103(D14):17099–110. doi:10.1029/98jd00900.

[58] Torres O, Jethva H, Bhartia PK. Retrieval of aerosol optical depth above clouds from OMI observations: sensitivity analysis and case studies. J Atmos Sci 2012;69(3):1037–53. doi:10.1175/jas-D-11-0130.1.

[59] van der Werf GR, Randerson JT, Giglio L, Collatz GJ, Mu M, Kasibhatla PS, Morton DC, DeFries RS, Jin Y, van Leeuwen TT. Global fire emissions and the contribution of deforestation, Savanna, forest, agricultural, and peat fires (1997–2009). Atmos Chem Phys 2010;10(23):11707–35. doi:10.5194/acp-10-11707-2010.

[60] Veefkind JP, et al. TROPOMI on the ESA Sentinel-5 Precursor: a GMES mission for global observations of the atmospheric composition for climate, air quality and ozone layer applications. Remote Sens Environ 2012;120:70–83. doi:10.1016/j.rse.2011.09.027.

[61] Wang J, Xu X, Ding S, Zeng J, Spurr R, Liu X, Chance K, Mishchenko M. A numerical testbed for remote sensing of aerosols, and its demonstration for evaluating retrieval synergy from a geostationary satellite constellation of GEO-CAPE and GOES-R. J Quant Spectrosc Radiat Transf 2014;146(0):510–28. doi:10.1016/j.jqsrt.2014.03.020.

[62] Waquet F, Riedi J, Labonnote LC, Goloub P, Cairns B, Deuzé JL, Tanré D. Aerosol remote sensing over clouds using A-train observations. J Atmos Sci 2009;66(8):2468–80. doi:10.1175/2009jas3026.1.

[63] Wielicki BA, et al. Achieving climate change absolute accuracy in orbit. Bull Am Meteorol Soc 2013;94(10):1519–39. doi:10.1175/BAMS-D-12-00149.1.

[64] Wilcox EM. Stratocumulus cloud thickening beneath layers of absorbing smoke aerosol. Atmos Chem Phys 2010;10(23):11769–77. doi:10.5194/acp-10-11769-2010.

[65] Wilcox EM. Direct and semi-direct radiative forcing of smoke aerosols over clouds. Atmos Chem Phys 2012;12(1):139–49. doi:10.5194/acp-12-139-2012.

[66] Wilcox EM, Harshvardhan, Platnick S. Estimate of the impact of absorbing aerosol over cloud on the MODIS retrievals of cloud optical thickness and effective radius using two independent retrievals of liquid water path. J Geophys Res 2009;114:D05210. doi:10.1029/2008JD010589.

[67] Wind G, Platnick S, King MD, Hubanks PA, Pavolonis MJ, Heidinger AK, Yang P, Baum BA. Multilayer cloud detection with the MODIS near-infrared water vapor absorption band. J Appl Meteorol Climatol 2010;49(11):2315–33. doi:10.1175/2010jamc2364.1.

[68] Xu F, et al. Coupled retrieval of liquid water cloud and above-cloud aerosol properties using the Airborne Multiangle SpectroPolarimetric Imager (AirMSPI). J. Geophys Res 2018;123(6):3175–204. doi:10.1002/2017JD027926.

[69] Xu X, Wang J. Retrieval of aerosol microphysical properties from AERONET photopolarimetric measurements: 1. Information content analysis. J Geophys Res 2015;120:7059–78. doi:10.1002/2015JD023108.

[70] Xu X, Wang J, Wang Y, Zeng J, Torres O, Yang Y, Marshak A, Reid J, Miller S. Passive remote sensing of altitude and optical depth of dust plumes using the oxygen A and B bands: first results from EPIC/DSCOVR at Lagrange-1 point. Geophys Res Lett 2017;44(14):7544–54. doi:10.1002/2017GL073939.

[71] Xu X, et al. Retrieval of aerosol microphysical properties from AERONET photopolarimetric measurements: 2. A new research algorithm and case demonstration. J Geophys Res 2015;120:7079–98. doi:10.1002/2015JD023113.

[72] Yu H, Zhang Z. New Directions: emerging satellite observations of above-cloud aerosols and direct radiative forcing. Atmos Environ 2013;72:36–40. doi:10.1016/j.atmosenv.2013.02.017.

[73] Zhang R, Khalizov AF, Pagels J, Zhang D, Xue H, McMurry PH. Variability in morphology, hygroscopicity, and optical properties of soot aerosols during atmospheric processing. Proc Natl Acad Sci 2008;105(30):10291–6. doi:10.1073/pnas.0804860105.

[74] Zhang Z, Meyer K, Platnick S, Oreopoulos L, Lee D, Yu H. A novel method for estimating shortwave direct radiative effect of above-cloud aerosols using CALIOP and MODIS data. Atmos Meas Technol 2014;7(6):1777–89. doi:10.5194/amt-7-1777-2014.